Neutron transfer in the ^{13}C + ^{197}Au reaction from gold isotope residuals

B. H. Daub,[1,2] D. L. Bleuel,[2,*] M. Wiedeking,[3] L. A. Bernstein,[1,2,4] N. M. Brickner,[1] J. A. Brown,[1]
B. L. Goldblum,[1] K. S. Holliday,[2] J. Lundgren,[1] and K. Moody[2]

[1]*University of California, Berkeley, California 94720, USA*
[2]*Lawrence Livermore National Laboratory, Livermore, California 94551, USA*
[3]*iThemba LABS, P.O. Box 722, 7129 Somerset West, South Africa*
[4]*Lawrence Berkeley National Laboratory, Berkeley, California 94720, USA*

Residual gold nuclei were produced via neutron transfer at multiple energies using a 130-MeV ^{13}C beam incident on a stacked-foil target consisting of alternating layers of ^{197}Au and ^{27}Al. Production cross sections, over an energy range of 56 to 129 MeV, for seven gold isotopes and two gold isomers were determined through activation analysis. By using the Wilczyński binary transfer model with a modified version of the recoil formula and a standard evaporation model, we were able to reproduce the isotopic production cross sections at high beam energy, with some disagreement at lower beam energies. This limiting angular momentum model does not predict the transfer of sufficient angular momentum to reproduce the observed isomeric populations.

I. INTRODUCTION

Heavy-ion fusion [1,2] followed by neutron evaporation has been a successful tool for studying the spectroscopic properties of nuclei at high spin and excitation energy. Its main limitation is the difficulty to reach the vast majority of neutron-rich nuclei due to the relative ease of neutron emission versus proton emission. Nonetheless, such nuclei have become increasingly important for nuclear structure and nuclear astrophysics studies over the last decades. Spectroscopic studies of nuclei with extreme nucleonic asymmetries have become accessible not only through a variety of methods, such as fragmentation [3], deep-inelastic [4], and fission reactions [5], but also through the use of many different massive transfer reactions in which the beam transfers several nucleons to the target nucleus [6–9]. This has traditionally involved using weakly bound nuclei such as ^{7}Li or ^{9}Be, where, respectively, a triton or ^{5}He nucleus is transferred to the target nucleus, ejecting an α particle, or vice versa. These massive-transfer reactions were studied using strongly bound projectiles such as ^{12}C, ^{14}N, and ^{16}O [10–14]. These type of reactions are also successfully used now with radioactive ion beams [15].

The spectrum of ejectiles is typically used when studying these massive-transfer reactions to determine the cross sections of different channels in the binary reaction, then characterized with an applicable reaction model. Over the years a number of models have been utilized to characterize multinucleon transfer. For instance the semiclassical GRAZING model [16,17] is popular for describing few-nucleonic transfer in heavy-ion reactions. More successful at predicting multinucleon transfer is the Zagrebaev model [18] which has been extensively used to describe superheavy element formation [19], but has also been applied to the production of lighter elements [20]. Another widely used approach is a sum-rule model first developed by Wilczyński *et al.* [13,14].

While this model has been successful in reproducing cross sections for cluster transfer channels [14], it has previously failed to predict the few-nucleon transfer cross sections for tightly bound projectiles such as ^{14}N. Additionally, the model does not explain the relation between the angle of α emission and neutron evaporation seen in ^{11}B + ^{176}Yb and ^{9}Be + ^{208}Pb reactions [7]. Most experiments focus on ejectile-γ coincidence measurements to identify residual nuclei. In this paper, we take a different approach through quantitative measurements of residuals using activation analysis.

We have performed a systematic measurement of the production of up to seven gold isotopes and two gold isomers from the ^{13}C + ^{197}Au reaction at seven energies. These energies range from 4.2 to 10 MeV/u, from just below to over twice the 56.6-MeV Coulomb barrier. The probability of nucleon exchange has been observed [21] to have an exponential dependence on the Q value. ^{13}C was chosen as a beam which enhances few-nucleon transfer while also yielding large spin transfers for isomer production. Both single-neutron transfer to and pickup from ^{197}Au have positive Q values, while other candidates in this mass region (e.g., ^{10}B, ^{11}B, ^{12}C, ^{14}N, and ^{16}O) have large negative Q values for one or both reactions. Gold was chosen as the target since it is monoisotopic and has a large number of long-lived radioactive isotopes and isomers for radiochemical analysis. Additionally, due to the high number of stable mercury isotopes, most of the nuclei of interest cannot be produced by the β decay of a higher Z isotope produced through fusion or incomplete fusion reactions.

In this experiment a ^{13}C beam was used to produce activated gold isotopes which are identifiable from the characteristic energies of γ rays emitted. After irradiation, the gold isotopes were chemically isolated and placed in front of high-purity germanium detectors. Dozens of characteristic-energy γ rays emitted following β, positron, electron-capture, or isomeric decay of the radioactive products were detected and used to identify residual quantities. Cross sections were determined from their activation and compared to models. Section II describes this experimental design, while Sec. III provides

*bleuel1@llnl.gov

details on the analysis and experimental results. In Sec. IV, we propose extensions to the Wilczyński model to improve its applicability to our observations. In Sec. V we fit parameters of this model to our data and interpret the results within the framework of statistical model calculations.

II. EXPERIMENTAL SETUP

A. Samples and irradiation

The experiment was performed at the Lawrence Berkeley National Laboratory's 88-in. cyclotron using a 70-pnA, 130-MeV ^{13}C beam. The beam was incident on a stack of alternating layers of thin gold and aluminum foils. The aluminum foils served as degraders, decreasing the ^{13}C energy between each gold foil. Table I shows the layered target configuration, mean energy determined from the beam energy at the beginning and end of each layer, and energy loss in each of the foils.

Energy losses are calculated using the code ELAST [22], which uses stopping power and range tables of Ziegler *et al.* [23]. Energy uncertainties include 0.5% for the beam energy propagated through each foil, added in quadrature to the cumulative uncertainties both from energy straggling in each successive foil as calculated by ELAST and from foil and sputtering thickness uncertainties reported by the suppliers. Using this stacked-foil technique, the transfer cross sections were measured from beam energies ranging from just below the Coulomb barrier (4.2 MeV/u) to 10 MeV/u. After the seventh gold foil (foil 13), three layers of aluminum were added to stop the ^{13}C beam. The last gold foil served as a monitor for the production of ^{198}Au or ^{196}Au due to absorption of evaporation neutrons through ^{197}Au(n, γ) and ^{197}Au$(n, 2n\gamma)$

TABLE I. Target stack composition. The first ten foils consisted of gold layers deposited onto aluminum foils, while the gold layers of the remaining foils were floated. The beam stopped in foil 16, allowing the final gold foil to serve as a monitor for reactions induced by evaporated neutrons.

Foil No.	Material	Thickness (mg/cm^2)	Mean energy (MeV)	Energy loss (MeV)
1	Au	1.93 ± 0.10	129.3 ± 0.7	1.36
2	Al	6.8 ± 1.0	124.4 ± 0.9	8.39
3	Au	1.93 ± 0.10	119.5 ± 1.5	1.44
4	Al	6.8 ± 1.0	114.3 ± 1.7	8.93
5	Au	2.32 ± 0.11	109.0 ± 2.1	1.83
6	Al	6.8 ± 1.0	103.6 ± 2.3	9.63
7	Au	1.93 ± 0.10	97.6 ± 2.7	1.63
8	Al	6.8 ± 1.0	91.5 ± 2.9	10.5
9	Au	1.93 ± 0.10	85.4 ± 3.4	1.77
10	Al	6.8 ± 1.0	78.7 ± 3.6	11.7
11	Au	1.9 ± 0.5	71.8 ± 4.3	1.96
12	Al	6.8 ± 1.0	64.2 ± 4.5	13.4
13	Au	1.9 ± 0.5	56.3 ± 5.5	2.22
14	Al	6.8 ± 1.0	47.1 ± 5.8	16.3
15	Al	6.8 ± 1.0	28.1 ± 7.6	21.6
16	Al	6.8 ± 1.0	8.7 ± 11.0	17.3
17	Au	1.9 ± 0.5	0	0.00

reactions. These contributions, which were observed to be very small, were subtracted from the measurements of the other foils.

This method was used to expose all foils to an identical beam profile in time, minimizing systematic uncertainties between each foil. At the maximum possible recoil energy, all gold nuclei produced were stopped in the aluminum layer immediately behind it. Therefore, each set of gold and aluminum foils was processed and counted using high-purity germanium (HPGe) detectors together.

The first ten foils were fabricated by depositing 1.93(10) mg/cm^2 gold layers [except foil 5 which was 2.32(11) mg/cm^2] onto 6.8(10)-mg/cm^2-thick aluminum substrates with the argon sputtering technique in a GATAN PECS model 682 [24]. Argon ions in a vacuum were accelerated toward a gold sample liberating gold atoms from the surface which coated all surfaces in the interior of the chamber. The thickness of the deposit was monitored with a piezoelectric quartz crystal microbalance within the sputter chamber, assuming uniform gold deposition. The last three 1.9(5)-mg/cm^2-thick gold layers (foils 11, 13, and 17) were floated onto 6.8(10)-mg/cm^2-thick aluminum backings.

The argon-sputtered, micron-thick gold layers were made and assayed in multiple steps. While the variation of individual layer thicknesses are ordinarily very small, the stated uncertainties reflect the compounding of individual deposition cycles. Free-standing foil thickness values are as reported by the manufacturer.

The foil stack was mounted on a water-cooled copper plate, which was electrically isolated from the beam line and connected to a current integrator, measuring the total number of incident ^{13}C particles. The time profile of the beam was measured by the rate of fusion-evaporation neutrons detected in a neutron monitor mounted outside the copper target and normalized using the total integrated current. Other than for a brief period early in the experiment, the beam current was relatively stable near 70 pnA and was assumed to be constant during the 13-h irradiation for the purpose of calculating the decay during production.

B. Chemical separation and counting of activated samples

Following irradiation the samples were transported to the low-background nuclear counting facility (NCF) [25] at Lawrence Livermore National Laboratory. The NCF is located underground, with HPGe detectors surrounded in 10 cm of pre-WWII lead, minimizing contributions from environmental radiation. Samples were counted sequentially on a single HPGe detector in a consistent geometry to minimize systematic uncertainties. A customized program, GAMANAL [26,27], performed background subtractions and peak fits, correcting for detector efficiency, sample geometry, dead time, coincidence loss, and self-shielding of γ rays in the samples. The detectors are regularly calibrated against NIST-traceable, multienergy point sources and large-area distributed sources.

The gold was chemically separated because of high background contributions from fusion-evaporation residue. Each pair of gold and aluminum foils was placed in a 40-ml centrifuge cone and dissolved with 2 ml 9M HCl and 6 drops
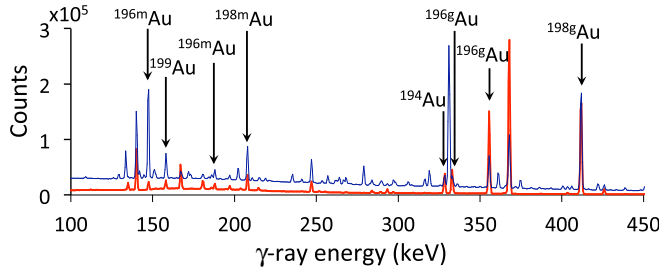
FIG. 1. A portion of the characteristic γ-ray spectra from foil 1, counted for 2 h. The spectra were taken before (blue, top) and after (red, bottom) chemical separation. Peaks labeled indicate the gold isotopes.

8M nitric acid. The samples were placed in a hot-water bath under air streams and evaporated to dryness. The dry deposits were dissolved in 0.5 ml 9M HCl and again evaporated to dryness. Each sample was dissolved in 3 ml 6M HCl, and 2 ml of ethyl acetate was added. The mixture was agitated for 90 s on a vortex mixer. The phases were allowed to settle, and the organic phase was transferred to a second 40-ml cone. Another 2 ml of ethyl acetate was added to the aqueous phase, and the agitation was repeated. The resulting organic phase was combined with the previous. Then 1 ml 6M HCl was added to the organic phase and the mixture was agitated for 60 s after which the aqueous phase was discarded. The clean organic phase, containing the gold activity, was evaporated to dryness under an air stream, dissolved in 1M HCl, and quantitatively transferred to a Prindle counting vial in 10 ml of dilute HCl.

The chemical separation improved the signal-to-background ratio, as shown in Fig. 1, by orders of magnitude in many cases. The absolute efficiencies of separation, typically on the order of 90%, were determined individually for the foils by comparing the ^{196g}Au activity measured before and after separation. Besides gold, isotopes of thallium and some lighter fission products such as gallium, molybdenum, and antimony could not be completely removed.

III. ANALYSIS AND RESULTS

A straightforward calculation of cross sections from measured activities was not possible due to multiple activated products feeding the same isotope. For instance, ^{198}Au decays with a 2.7-day half-life into ^{198}Hg producing primarily a 411-keV γ-ray transition. However, thallium was still detected in the sample with approximately the same chemical separation efficiency as gold. ^{198}Tl decays by electron capture also to ^{198}Hg, producing the same γ ray but with a half-life of 5.3 h. The isotope ^{198}Tl itself is continuously produced by the decay of ^{198}Pb. Furthermore, the ground state of ^{198}Au is additionally fed by the decay of its 2.3-day high-spin isomer at 812 keV. This entire decay network must be carefully considered when determining the ^{198g}Au production cross section. By measuring the activity in five time intervals following chemical separation, the contribution of each decay chain could be determined.

Analysis of multiple decay chains and interfering γ rays was performed using linear algebra to decouple direct
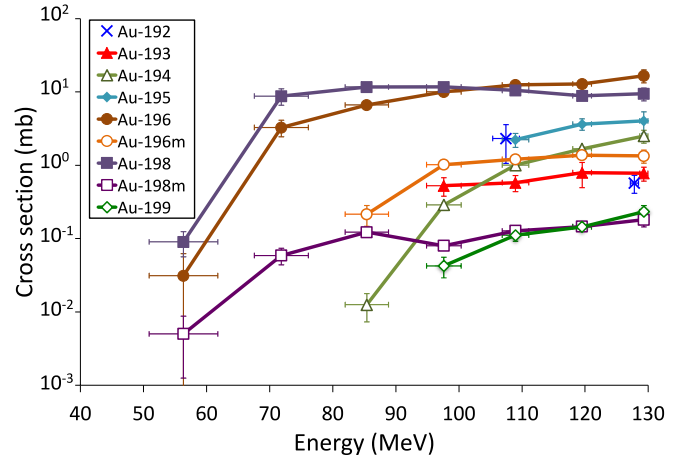

FIG. 2. Residual gold production cross sections (data points) as a function of ^{13}C energy in the laboratory frame. Connecting lines are added only to guide the eye. Data points for ^{192}Au have been slightly downshifted in energy for clarity (see text for details).

production of a daughter nucleus from ingrowth due to a parent nucleus. From this, the activities are converted to γ-ray intensities [28–34] and compared to the measured γ-ray rates. At each incident energy a system of matrix equations is set up and diagonalized that contain the decay equations, cross sections, and reaction channels. These matrices are on the order of 100×100 in dimension, due to the large number of reaction channels in excess of just the gold isotope production and decay. The number of initial nuclei of each product was used as a fit parameter in a χ^2 minimization to determine the cross sections.

Cross sections as a function of energy for each of the gold isotopes and isomers observed are shown in Fig. 2 and listed in Table II. The cross sections are largely independent of energy once they have reached their peak value. For ^{192}Au the 4.9-h half-life represents the limit of our ability to reliably detect the decays. The number of counts in that isotope's primary characteristic peak for the foil receiving a beam energy of 119.5(15) MeV was so low that a good fit over the background could not be attained and the uncertainty in the production cross section was much larger than its value, thus not deemed a reliable enough measurement to report. This is also evident by the larger uncertainties of neighboring cross sections. Nonetheless we have chosen to retain the data to not subjectively bias our analysis when possible peaks could be detected. The half-lives of the other studied isotopes were long enough to yield sufficient statistics.

The cross-section uncertainties were determined from the Hessian matrix [35], composed of the second derivatives of the χ-squared function with respect to all pairs of parameters. The error matrix is then given by the inverse of the Hessian matrix. Energy uncertainties are as described in Sec. II.

IV. EXTENSION OF THE WILCZYŃSKI MODEL

The presence of ^{199}Au indicates multiple neutron transfers. The detection of a significant amount of ^{7}Be, identified through the 477.6-keV γ-ray emission, in the monitor foil (foil 17) im-

TABLE II. Residual gold production cross sections in units of millibarn for average ^{13}C energies ($\overline{E}$) in each foil.

Nucleus	$\overline{E}$ (MeV)						
	56.3 ± 5.5	71.8 ± 4.3	85.4 ± 3.4	97.6 ± 2.7	109.0 ± 2.1	119.5 ± 1.5	129.3 ± 0.7
^{192}Au					2.3 ± 1.3		0.57 ± 0.16
^{193}Au				0.53 ± 0.15	0.58 ± 0.14	0.79 ± 0.30	0.78 ± 0.17
^{194}Au			0.013 ± 0.005	0.29 ± 0.02	1.01 ± 0.05	1.68 ± 0.09	2.5 ± 0.5
^{195}Au					2.2 ± 0.5	3.7 ± 0.6	4.0 ± 1.3
^{196m}Au			0.22 ± 0.07	1.0 ± 0.1	1.2 ± 0.1	1.4 ± 0.1	1.3 ± 0.3
^{196g}Au	0.031 ± 0.032	3.3 ± 0.8	6.7 ± 0.3	10.0 ± 0.5	12.5 ± 0.6	12.9 ± 0.7	17 ± 3
^{198m}Au	0.0050 ± 0.0038	0.059 ± 0.015	0.122 ± 0.008	0.080 ± 0.006	0.128 ± 0.009	0.15 ± 0.01	0.18 ± 0.04
^{198g}Au	0.090 ± 0.034	8.8 ± 2.2	11.7 ± 0.6	11.8 ± 0.6	10.5 ± 0.5	8.9 ± 0.5	9.4 ± 1.9
^{199}Au				0.043 ± 0.013	0.11 ± 0.02	0.15 ± 0.02	0.23 ± 0.05

plies some breakup of the incident beam and possible capture of fragments by the target. The direct breakup of ^{13}C into ^{7}Be and ^{6}He, with a Q value of -30.2 MeV, is energetically possible at the center-of-mass energy of 122 MeV. However, a more probable source of ^{7}Be is two-neutron stripping, which is likely to be a dominant process. The stripping reaction could produce excited ^{11}C* above its breakup threshold into ^{7}Be and ^{4}He of 7.5 MeV. The binary transfer model developed by Wilczyński *et al.* includes these processes and has previously been applied to the spectra of ejectiles from reactions at 10 MeV/u [13,14]. This model treats all reactions as two body, in which one or more nucleons are transferred. All channels, including those produced in complete fusion, are treated identically and the decay of the excited residual nuclear state is independent of the entrance channel.

However, as discussed in Sec. I, most experimental comparisons with this model inferred the reaction from outgoing projectiles and not the production of residual nuclei. Traditionally, the model has only successfully fit the α channels while neutron transfer channels have yielded relatively poor fits [14]. Therefore, extensions to the Wilczyński model are tested to improve agreement with our measurements.

The Wilczyński model has previously been fitted to experimental reaction data [14] with the free parameters of temperature (T), a transmission coefficient cutoff parameter (Δ_ℓ), an effective charge interaction radius (R_c), and a dissipation energy (E_{diss}). The first three parameters, T, Δ_ℓ, and R_c, are used to predict cross sections using a generalized concept of critical angular momentum. The last parameter, E_{diss}, is used to predict energy transfer in these neutron transfer reactions, determining the subsequent number of evaporation neutrons. We use a best fit of the measured cross sections presented in Sec. III to this model, modified to the specifics of these reactions. A new set of these four parameters for neutron transfer from ^{13}C to the gold system is determined. We then discuss the quality of fit and implications of each parameter.

A. Binary transfer cross section and critical angular momentum

The Wilczyński model prediction of angular momentum transfer in this reaction was initially insufficient to predict the observed high-spin (12^-) isomer populations of ^{196m}Au ($E_x = 595.7$ keV and $T_{1/2} = 9.6$ h) and ^{198m}Au ($E_x = 811.7$ keV

and $T_{1/2} = 2.272$ d) and a more comprehensive treatment of angular momentum was deemed necessary. For our analysis, the angular momentum and excitation energy transferred to the residual nucleus are much more critical, because we cannot differentiate between the production of the same residual nucleus by different channels, for example, a pickup reaction and a stripping reaction followed by evaporation [e.g., ^{197}Au(^{13}C,^{14}C)^{196}Au vs ^{197}Au(^{13}C,^{12}C + $2n$)^{196}Au].

In the original Wilczyński model, the total cross section for each channel, i, is given by

$$\sigma(i) = \frac{\pi \hbar^2}{2\mu E} \sum_{\ell=0}^{\ell_{\max}} (2\ell + 1) T_\ell(i) p(i) N_\ell, \tag{1}$$

where $\hbar^2/2\mu E$ is the reduced wave length, $T_\ell(i)$ is the transmission coefficient for channel i and angular momentum ℓ, $p(i)$ is the probability of a binary reaction into channel i, and N_ℓ is a normalization factor for each ℓ, expressions for each of which are given in Ref. [14].

The angular momentum transfer to the residual for a given incoming ℓ has previously been assumed to follow only the ℓ-matching condition of

$$\ell_{\text{trans}} \approx \frac{A_c}{A_p} \ell, \tag{2}$$

where A_p and A_c are the mass numbers of, respectively, the projectile and captured fragment. However, this neglects the spin of both the projectile and ejectile, and to account for these, we convert the sum over ℓ in Eq. (1) to sums over J, j, and ℓ,

$$\sigma(i) = \frac{\pi \hbar^2}{2\mu E} \sum_{J=0}^{\ell_{\max}+I+S} \frac{(2J + 1)}{(2I + 1)(2S + 1)}$$
$$\times \sum_{j=|J-I|}^{J+I} \sum_{\ell=|j-S|}^{j+S} T_\ell(i) p(i) N_\ell, \tag{3}$$

where J is the total angular momentum, I is the spin of the target, S is the spin of the projectile, and j is the total angular momentum of the projectile. After the transfer, we still assume that the ejectile orbital angular momentum is given by $\ell' = \ell - \ell_{\text{trans}}$, and add the sum over the ejectile total angular

momentum j',

$$\sigma(i) = \frac{\pi \hbar^2}{2\mu E} \sum_{J=0}^{\ell_{\max}+I+S} \frac{(2J+1)}{(2I+1)(2S+1)}$$

$$\times \sum_{j=|J-I|}^{J+I} \sum_{\ell=|j-S|}^{j+S} T_\ell(i) p(i) N_\ell \sum_{j'=|\ell'-S'|}^{\ell'+S'} (2j'+1) N_{\ell'}, \quad (4)$$

where S' is the ejectile spin, and $N_{\ell'}$ is a normalization factor given by

$$N_{\ell'} \sum_{j'=|\ell_{\mathrm{trans}}-S'|}^{\ell_{\mathrm{trans}}-S'} (2j'+1) = 1. \quad (5)$$

The total angular momentum transferred to the residual nucleus is then $J - j'$. This keeps the primary assumption of the ℓ-matching model intact, while allowing all possible combinations of ℓ, I, S, S', and ℓ'.

B. Neutron evaporation using the optimum Q-value approach

For the energy transfer, previous experiments have either attempted to use an optimum Q value from velocity-matching conditions and nuclear friction, or assumed that the kinetic energy of the beam is transferred in proportion to the number of transferred nucleons.

The optimum Q-value approach predicts a maximum in the cross section for transfer of n nucleons from the projectile with mass number A_p to the target with mass number A_t, and of m nucleons in the other direction when the relative velocities before and after the transfer (v_i and v_f) satisfy the following recoil formula [36]:

$$v_f = \left(1 - \frac{n}{A_t - m + n} - \frac{m}{A_p - n + m}\right)v_i \equiv K v_i. \quad (6)$$

It is empirically observed that an additional term arises from dissipation of energy in the entrance channel, such that the optimum Q value is given by [14]

$$Q_{\mathrm{opt}} = U_f(R_{\mathrm{int}}) - E_0 + \frac{\mu_f}{\mu_i} K^2 [E_0 - U_i(R_{\mathrm{int}}) - E_{\mathrm{diss}}], \quad (7)$$

where $U(R_{\mathrm{int}})$ is the nuclear-plus-Coulomb potential at the interaction distance R_{int} [37], E_0 is the bombarding beam energy, μ is the reduced mass, and E_{diss}, the dissipation energy, is an empirically determined parameter. The subscripts i and f refer to the initial and final channels. For the system ^{14}N + ^{159}Tb at 10 MeV/u, E_{diss} was determined to be 10 MeV based on peak positions in ejective energy spectra [14].

We chose to hybridize the optimum Q-value approach and the equal distribution of kinetic energy approach. Rather than the constant value of $E_{\mathrm{diss}} = 10$ MeV, which was determined empirically for a single beam energy and a different reaction, we observe a best fit to our energy-dependent data with the assumption that it is proportional to the beam energy per nucleon. Based on the angular momentum and energy transferred for each channel from Eqs. (2) and (7), the

final residuals were calculated using the Hauser-Feshbach evaporation formalism [38] as implemented in the TALYS code [39].

V. FIT AND INTERPRETATION

Using the traditional Wilczyński formulation, the energy transfer from Eq. (7) for the ^{13}C + ^{197}Au system results in significant evaporation, and cannot reproduce the large ^{198}Au and ^{196}Au cross sections, indicating that there must be substantially less energy transferred. The best agreement between model and observation for ^{196}Au and ^{198}Au was reached with a decreased dissipated energy $E_{\mathrm{diss}} = 0.22 E_{\mathrm{beam}}$ MeV/u, as shown in Fig. 3. Other parameters were optimized to $T = 2.52$ MeV, $R_c = 12.7$ fm, and $\Delta_\ell = 5.11$ using the Nelder-Mead Simplex algorithm [40].

This model fails to predict any production of ^{192}Au, which is consistent with the reduced quality of our ^{192}Au measurement as discussed in Sec. III, and tends to underpredict the production of ^{193,194,195}Au. Including sufficient energy transfer in the model to predict ^{192}Au production leads to excessive evaporation of ^{196,198}Au and poor agreement with the production of those isotopes. This is most likely due to the limitation that we assume that all ejectile energies are fixed by Q_{opt}, while experimental measurements have shown a long tail in cross sections at lower ejectile energies [13].

The T and Δ_ℓ parameters in this work are consistent with parameters determined from previous measurements [8,14], lending support to the validity of our approach. However, the dissipated energy is found to be significantly less in our neutron transfer channels compared to those derived from the ^{14}N + ^{159}Tb system [14] at the equivalent beam energy. Replacing $E_{\mathrm{diss}} = 10$ MeV with $E_{\mathrm{diss}} = 0.22 \times 10$ MeV in the recoil
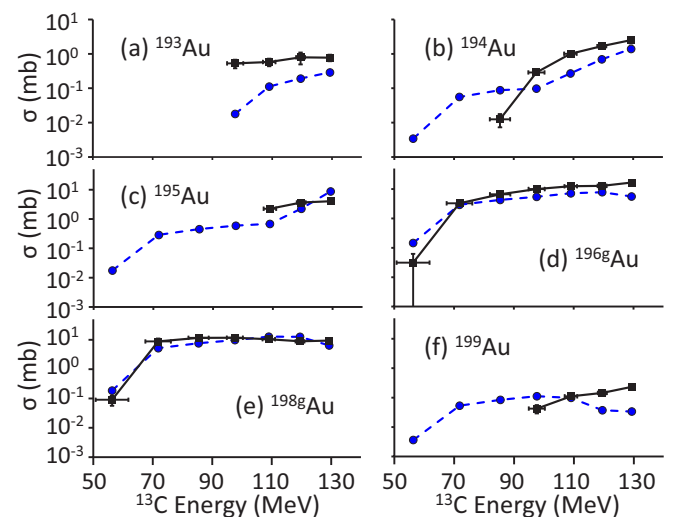
FIG. 3. Measured cross sections (black squares) versus those predicted from the Wilczyński binary transfer model (blue circles) with the assumption that the dissipated energy in the entrance channel is proportional to the beam energy per nucleon. Parameters are $T = 2.52$ MeV, $R_c = 12.7$ fm, $\Delta_\ell = 5.11$, and with $E_{\mathrm{diss}} = 0.22 E_{\mathrm{beam}}$ MeV/u. Calculations with zero cross-section values are not plotted. The ^{192}Au cross sections could not be reproduced using the binary transfer model.

formula reproduces the previously poor fit of the observed peak Q value for the $(^{14}N, ^{15}N)$ channel, which was the only pure neutron transfer channel reported.

This dissipation energy increases in proportion to the incoming beam energy, but is balanced by the increasing total reaction cross section. This results in cross sections which are largely independent of beam energy. Similar results have been reported for the residual production of $^{160-164}Dy$ following evaporation from the $^{160}Gd(^{7}Li, ^{3}H + xn)$ reaction [8] and the normalized residual production of ^{179}Ta and ^{180}Ta following evaporation from the $^{176}Yb(^{176}B, \alpha + xn)$ reactions [7].

Although there is no charge exchange in neutron transfer, all transfer channels were included in the global fit, resulting in an effective charge exchange distance (R_c) of approximately 12.7 fm. This value is similar to the interaction radius, though larger than the solid contact distance of 10 fm for this system. This is consistent with the decrease of E_{diss} compared to that of the $^{14}N + ^{159}Tb$ system at the equivalent beam energy. This dissipated energy is postulated to arise from strong radial nuclear friction [14]. The concept of nuclear friction represents the energy loss of a projectile as it traverses a nucleus. In models of nuclear friction, this energy dissipation is proportional to the overlap of the nuclei and the relative radial velocity [41–43], both of which are significantly lower in peripheral collisions.

The analysis of activated products from the one- and two-α particle emission channels could provide more information regarding the relative probability of charge transfer. Unfortunately, this is limited by the short half-lives of the relevant isotopes and ingrowth from the decay of fusion-evaporation products which are the dominant reaction channels.

Information on the angular momentum transfer is only seen indirectly through neutron evaporation and from the relative population of the two high-spin isomers ^{196m}Au and ^{198m}Au. Figure 4 shows the relative isomer population for both ^{196}Au and ^{198}Au versus energy compared with predicted relative populations using the TALYS and DICEBOX [44] codes for the statistical γ-ray cascades. The input into TALYS is the excitation energy and angular momentum distribution predicted by our modified Wilczyński model. TALYS uses the Hauser-Feshbach formalism [38] to calculate branches of neutron evaporation and uses average statistical properties to calculate electromagnetic quantities in the region of high level density to determine the subsequent γ-ray emission. The same initial excitation energy and angular momentum distribution, plus those generated by TALYS following neutron evaporation, are input into DICEBOX, which instead generates level structures from a constant-temperature model and the corresponding statistical γ-ray cascades using the Monte Carlo technique. Both codes transition from these models to measured discrete levels at low energy where knowledge of the level structure is assumed complete.

Due to the unknown level structure which feeds these isomers, the quasicontinuum level density of a "constant temperature + Fermi gas" model was used in both codes instead of the known discrete states above the isomer. Results did not change significantly when using a back-shifted Fermi gas model. Although our extension to the Wilczyński model improved the isomer population prediction relative to our
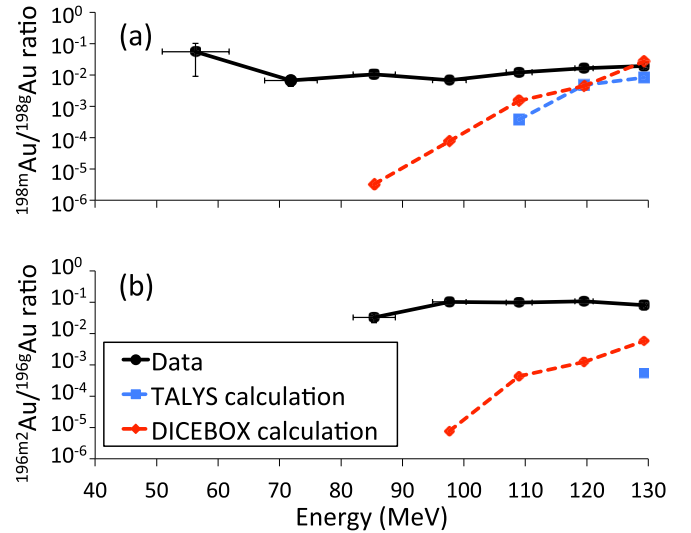

FIG. 4. Comparison of measured isomer to ground-state ratios (black circles) with those predicted using TALYS (blue squares) and DICEBOX (red diamonds) to calculate the statistical γ-ray cascade for both ^{198}Au (a) and ^{196}Au (b). Both isomers show much higher relative population in the data than is predicted by the binary transfer model, with a particularly large discrepancy from ^{196}Au. Calculations with zero cross-section values are not plotted.

observation, both the calculated statistical cascade from TALYS and the Monte Carlo generated level structures of DICEBOX still failed to reproduce the much higher relative population of the isomers. This is particularly evident in ^{196}Au, where the predictions differ by orders of magnitude. Additionally, both theoretical calculations show an increase in isomer population with energy, while the measured relative populations are nearly energy independent. Previous measurements [14] of the angular momentum transfer from single nucleon exchange also found that the predicted transfer from the binary ℓ-matching model is insufficient to explain the high angular momentum transfers observed. These results may be indicative of the possibility of other reaction mechanisms, requiring further investigation.

Both TALYS and DICEBOX significantly underestimate the isomer-to-ground state ratio. This may be due to an incomplete knowledge of the level structure at excitation energies above the high angular momentum isomers (both 12^-), which would result in discrepancies in the model output even if the initial excited-state angular momentum distribution is correct. Furthermore, the lack of a well-tested optical model for the ^{13}C-induced reaction may undermine the robustness of the angular momentum transfer into evaporation residues.

VI. SUMMARY

We have measured residual cross sections for seven isotopes and two isomers of gold following neutron transfer in the $^{13}C + ^{197}Au$ reaction. These results are well described by highly peripheral collisions with limited energy dissipation from nuclear friction using a modification of the binary transfer model developed by Wilczyński *et al.* [13,14]. This indicates

that significantly less energy is dissipated by nuclear friction in neutron transfer than in charged-particle transfer.

We have demonstrated the validity of the binary ℓ-matching model for the total cross section for one- and two-neutron transfer where it had previously yielded poor agreement [14]. However, the assumptions regarding angular momentum transfer from this model fail to reproduce the relative isomeric populations in ^{196}Au and ^{198}Au, though this failing may be due to a lack of knowledge of high-spin states above the isomers. Further work must be done to understand the relationship between residual excitation energy, angular momentum transfer, and the angle of the ejectile in order to fully exploit massive transfer reactions as a nuclear spectroscopy tool. Development of beams of neutron-rich light nuclei in this energy range will extend this capability to residual nuclei with larger neutron excess.

[1] B. B. Back, H. Esbensen, C. L. Jiang, and K. E. Rehm, Rev. Mod. Phys. **86**, 317 (2014).

[2] R. A. Broglia and A. Winther, *Heavy Ion Reactions: Parts 1 and 2 (Frontiers in Physics)* (Addison-Wesley, Reading MA, 1991).

[3] José Benlliure, J. Phys.: Conf. Ser. **312**, 082001 (2011).

[4] R. Broda, J. Phys. G: Nucl. Part. Phys. **32**, 151 (2006).

[5] A. Navin and M. Rejmund, Gamma-Ray Spectroscopy of Neutron-Rich Fission Fragments, AccessScience (2014), doi:10.1036/1097-8542.YB140316.

[6] T. Udagawa and T. Tamura, Phys. Rev. Lett. **45**, 1311 (1980).

[7] G. D. Dracoulis, A. P. Byrne, T. Kibédi, T. R. McGoram, and S. M. Mullins, J. Phys. G: Nucl. Part. Phys. **23**, 1191 (1997).

[8] R. M. Clark, L. W. Phair, M. Descovich, M. Cromaz, M. A. Deleplanque, P. Fallon, I. Y. Lee, A. O. Macchiavelli, M. A. McMahan, L. G. Moretto, E. Rodriguez-Vieitez, S. Sinha, F. S. Stephens, D. Ward, M. Wiedeking, L. A. Bernstein, J. T. Burke, and J. A. Church, Phys. Rev. C **72**, 054605 (2005).

[9] R. Yanez and W. Loveland, Phys. Rev. C **91**, 044608 (2015).

[10] T. Inamura, M. Ishihara, T. Fukuda, T. Shimoda, and H. Hiruta, Phys. Lett. B **68**, 51 (1977).

[11] K. Siwek-Wilczyńska, E. H. du Marchie van Voorthuysen, J. van Popta, R. H. Siemssen, and J. Wilczyński, Phys. Rev. Lett. **42**, 1599 (1979).

[12] K. A. Geoffroy, D. G. Sarantites, M. L. Halbert, D. C. Hensley, R. A. Dayras, and J. H. Barker, Phys. Rev. Lett. **43**, 1303 (1979).

[13] J. Wilczyński, K. Siwek-Wilczyńska, J. van Driel, S. Gonggrijp, D. C. J. M. Hageman, R. V. F. Janssens, J. Łukasiak, and R. H. Siemssen, Phys. Rev. Lett. **45**, 606 (1980).

[14] J. Wilczyński, K. Siwek-Wilczyńska, J. van Driel, S. Gonggrijp, D. C. J. M. Hageman, R. V. F. Janssens, J. Łukasiak, R. H. Siemssen, and S. Y. Van Der Werf, Nucl. Phys. A **373**, 109 (1982).

[15] S. Bottoni *et al.*, Phys. Rev. C **92**, 024322 (2015).

[16] A. Winther, Nucl. Phys. A **572**, 191 (1994).

[17] A. Winther, Nucl. Phys. A **594**, 203 (1995).

[18] V. I. Zagrebaev, Ann. Phys. (NY) **197**, 33 (1990).

[19] V. I. Zagrebaev and W. Greiner, Phys. Rev. C **87**, 034608 (2013).

[20] V. I. Zagrebaev, B. Fornal, S. Leoni, and Walter Greiner, Phys. Rev. C **89**, 054608 (2014).

[21] A. G. Artukh, V. V. Avdeichikov, J. Erö, G. F. Gridnev, V. L. Mikheev, V. V. Volkov, and J. Wilczynski, Nucl. Phys. A **160**, 511 (1971).

[22] Energy Loss and Straggling Tool, adapted from the computer program ENELOSS, written by H. Ernst (1981) modified by K. Lesko (1984).

[23] J. F. Ziegler, J. P. Biersack, and U. Littmark, *The Stopping and Ranges of Ions in Matter*, Vol. 1 (Plenum, New York, 1985).

[24] Product catalog http://glteam.com/pdf/682PECS(New).pdf (retrieved 2016).

[25] *Nuclear Counting Facility Detector Calibration Procedure for the Forensic Science Center*, LLNL-TM-427812, FSC-SOP-26, Rev. 3 (2010).

[26] R. Gunnick and J. B. Niday, UCRL-51061, Vols. 1–4, LLNL (1971–1972).

[27] R. Gunnick, W. D. Ruhter, and J. B. Niday, UCRL-53861, Vols. 1–3 (1988).

[28] Coral M. Baglin, Nucl. Data Sheets **113**, 1871 (2012).

[29] E. Achterberg, O. A. Capurro, G. V. Marti, V. R. Vanin, and R. M. Castro, Nucl. Data Sheets **107**, 1 (2006).

[30] B. Singh, Nucl. Data Sheets **107**, 1531 (2006).

[31] H. Xiaolong and K. Mengxiao, Nucl. Data Sheets **121**, 395 (2014)

[32] H. Xiaolong, Nucl. Data Sheets **108**, 1093 (2007).

[33] H. Xiaolong, Nucl. Data Sheets **110**, 2533 (2009).

[34] B. Singh, Nucl. Data Sheets **108**, 79 (2007).

[35] W. R. Leo, *Techniques for Nuclear and Particle Physics Experiments* (Springer-Verlag, Berlin, 1994).

[36] P. J. Siemens, J. P. Bondorf, D. H. E. Gross, and F. Dickmann, Phys. Lett. B **36**, 24 (1971).

[37] W. U. Schroder and J. R. Huizenga, Annu. Rev. Nucl. Sci. **27**, 465 (1977).

[38] W. Hauser and H. Feshbach, Phys. Rev. **87**, 366 (1952).

[39] A. J. Koning, S. Hilaire, and M. C. Duijvestijn, TALYS-1.0, in *Proceedings of the International Conference on Nuclear Data for Science and Technology, 22-27 April 2007, Nice,*

France, edited by O. Bersillon, F. Gunsing, E. Bauge, R. Jacqmin, and S. Leray (EDP Sciences, 2008), p. 211 (see also http://www.talys.eu).

[40] J. A. Nelder and R. Mead, Comput. J. **7**, 308 (1965).

[41] D. H. E. Gross and H. Kalinowski, Phys. Lett. B **48**, 302 (1974).

[42] J. Wilczyński, K. Siwek-Wilczyńska, J. S. Larsen, J. C. Acquadro, and P. R. Christensen, Nucl. Phys. A **244**, 147 (1975).

[43] D. H. E. Gross and H. Kalinowski, Phys. Rep. **45**, 175 (1978).

[44] F. Bečvář, Nucl. Instrum. Methods Phys. Res., Sect. A **417**, 434 (1998).